

UNCLASSIFIED

Defense Technical Information Center  
Compilation Part Notice

ADP011111

**TITLE:** Thrust Vectoring for Advanced Fighter Aircraft - High Angle of Attack Intake Investigations -

**DISTRIBUTION:** Approved for public release, distribution unlimited

This paper is part of the following report:

**TITLE:** Active Control Technology for Enhanced Performance Operational Capabilities of Military Aircraft, Land Vehicles and Sea Vehicles  
[Technologies des systemes a commandes actives pour l'amelioration des performances operationnelles des aeronefs militaires, des vehicules terrestres et des vehicules maritimes]

To order the complete compilation report, use: ADA395700

The component part is provided here to allow users access to individually authored sections of proceedings, annals, symposia, etc. However, the component should be considered within the context of the overall compilation report and not as a stand-alone technical report.

The following component part numbers comprise the compilation report:

ADP011101 thru ADP011178

UNCLASSIFIED

# Thrust Vectoring for Advanced Fighter Aircraft

## - High Angle of Attack Intake Investigations -

Dr. Norbert C. Bissinger

Michael Jost

DaimlerChrysler Aerospace AG

Military Aircraft Division

P.O. Box 80 11 60

81663 Munich, Germany

### Abstract

In this paper the results of investigations will be presented which dealt with the determination of intake flows at high and very high angles of attack. The overall approach comprised of experimental and numerical (CFD) investigations will be detailed. Results and comparisons between flows at small and large angles of attack will be used to try to clarify the origin of possible disturbances in the intake flow. Intake bleed and the flow losses at the intake entrance are identified as major components contributing to the quality of the intake flow at the engine face

### Nomenclature

A0/AC	area ratio of streamtube area A0 and intake capture area AC
AIP	aerodynamic interface plane (engine face)
Cp	pressure coefficient
DC60	steady state distortion parameter
DC60TA	instantaneous distortion parameter
$\dot{m}$	engine mass flow per unit time
Ma	Mach number
pt0	free stream total pressure
pt2	engine face total pressure
Rmax	engine face radius
Tt	total temperature
WAT	normalized engine mass flow
	$\dot{m} * \sqrt{Tt} / pt_1$
$\alpha$	angle of attack
$\eta$	intake pressure recovery ( $pt_2/pt_0$ )
$\delta_1$	vari-cowl angle
$\theta_1$	foreplane angle

### 1. Introduction

Thrust vectoring has the potential to improve the performance of fighter aircraft throughout the flight envelope. Major performance improvements could be achieved when, e.g., using thrust vectoring for trimming the aircraft, especially in the supersonic flight regime, or when using thrust vectoring in case of failure or loss of a control surface and most importantly when using thrust vectoring for the enhancement of the manoeuvrability/agility in the subsonic flight regime including poststall.

Higher agility and flight in the poststall regime in general is connected with angles of attack which are far out of the range for a conventional aircraft without thrust vectoring. The angle of attack range is definitely beyond that for which the intake

usually is designed for. Therefore it must be ensured that at these high angles of attack the flow inside the intake will not be deteriorated so much that serious intake/engine compatibility problems would occur. These problems could lead not only to thrust losses at very critical flight situations but could also result in damages of the engine and/or aircraft due to the very high pressure loads connected with malfunctioning (surge) of the engine.

### 2. Aim of the investigations

When implementing a novel technology like thrust vectoring into an existing aircraft it is desirable to do this with as little changes to the aircraft design as possible. It would even be appreciated if no changes at all would become necessary. However this would only be possible if the existing intake design could be proven to deliver sufficient air mass flows with limited distortion and swirl to the engine not only within its design range but also at very high angles of attack. It was therefore decided to perform a windtunnel investigation with an existing windtunnel model without any modifications mainly in the extended angle of attack range. With this windtunnel investigation the performance of the intake in this extended range was to be demonstrated. With the data collected further work was to be identified and modifications to the intake were to be derived if considered necessary.

Numerical flow calculations (CFD) were to be performed to support the analysis of the windtunnel data.

### 3. Airplane/intake configuration considered

As an example for a modern fighter aircraft for which in Refs. [1 and 2] different aspects of the implementation of thrust vectoring have been investigated the Eurofighter (Typhoon) has been selected. This fighter is very powerful in the medium range and close-in air combat range. It also possesses an excellent secondary Air-to-Ground capability. In addition it has been designed for high superiority in the supersonic range. The configuration which is able to satisfy all these requirements is a Delta Wing configuration with all-moveable 'long-coupled' Canard foreplanes. The aircraft is powered by two EJ200 engines supplied with air by two side-by side chin intakes.

The shape of the intake entrance from a front-view is a rectangle which has been curved like the bottom of the fuselage (smiling intake). At supersonic flight Mach numbers a ramp which is separated from the fuselage by a diverter produces an oblique shock in order to decelerate the flow. The leading edge of the splitter plate separating the two intakes is located downstream of this oblique shock. For low Mach

number and for high angle of attack operation a variable cowl lip (vari-cowl) has been implemented into the design. Because of the vari-cowl no auxiliary intake doors are necessary. Only in the side-view some S-shape curvature of the intake duct can be recognized in fig. 3.1. Viewed from the top the intake duct is more or less straight.

For the stabilization of the shock system at supersonic Mach numbers a bleed system (porous wall) has been incorporated on the intake ramp. For the improvement of the intake flow (reduced distortion) air is dumped via an intake bleed slot on the ramp side downstream of the intake throat.

#### 4. Wind tunnel investigation

##### 4.1 Intake model

The intake model that has been used during these investigations is shown in fig. 4.1.1. Its scale is 1: 10.32. Only the forward part of the wing has been reproduced on this model. This can be justified by the fact that at the high angles of attack to be tested the intake on-set flow will be dominated by the shielding of the fuselage and the canard.

During all the testing the intake lip position has been held fixed at its most open position (which has been determined for the highest angles of attack considered sofar). Also the canard position has not been changed after pre-tests had proven that the canard position depicted a negligible influence on the intake performance (largest 'nose-down' position).

The intake mass flow has been varied between very low and very high values with the help of an ejector system at the exit of the two intake ducts.

##### 4.2 Windtunnel

The model has been tested in the ONERA-S1MA windtunnel in Modane (France). This windtunnel is ideally suited for such testing because the large size of its test-section (about  $40 \text{ m}^2$ ) allows testing at extreme angles of attack without undue windtunnel wall interferences. The only limitation existing may be the power of the windtunnel Pelton turbines.

##### 4.3 Test program and test data

The test program is given in table 1. The angles of attack ranged from  $20^\circ$  to  $110^\circ$ , the Mach numbers from 0.3 to 0.8. For nearly all test points sideslip angle has been kept at zero with one exception at  $\text{Ma} = 0.3$  where a sideslip angle of  $\pm 10^\circ$  has been investigated.

For the determination of the steady state intake performance in the port intake AIP (aerodynamic interface plane  $\cong$  engine face plane) a rake for the measurement of swirl and pressure recovery has been used. The five-hole probes and the pitot probes are arranged on different rake arms. Their position can be recognized in fig. 4.3.1. There exist 8 rake arms with 7 pitot probes and 8 rake arms with 2 five-hole probes. The flow angularity (swirl) is measured on two rings in the outer part of the intake AIP only. In the starboard intake AIP a fully dynamic rake for the measurement of dynamic distortion has been mounted (see fig. 4.3.2). Steady state total pressure with this rake is measured with the help of 16 rake arms with 5 pitot probes. For the dynamic total pressure on every second rake arm Kulites have been mounted on the side of the steady state pitots.

With these two rakes steady state pressure recovery can be calculated as the area weighted mean of the pitot pressures. The parameter swirl as used here is the arithmetic mean of the 8 circumferential flow angles on the outer most ring on which five-hole probes are located. Viewed from the front of the intake positive swirl is rotating clock-wise. Distortion DC60 is a measure for the "distortion" of the total pressure distribution in the AIP (and therefore for the flow losses within the intake duct flow). The areas where total pressures below the AIP mean occur are screened for the  $60^\circ$  sector with minimum mean total pressure. DC60 then is the difference between the (minimum) total pressure of this sector and the AIP mean total pressure scaled by the dynamic pressure in the AIP. For the determination of the dynamic distortion DC60TA the same calculation procedure is used with the time-dependent pitot pressure signals. (Details of the data reduction of these dynamic pressure signals are omitted here). Mass flows at the AIP, the ramp bleed and the intake slot bleed have been measured and are given in the form of an area ratio  $A0/AC$  or as WAT. At various stations on the fuselage and at intake walls steady state and dynamic wall pressures have been measured.

##### 4.4 Data analysis

During the first test runs data points from former windtunnel entries were repeated in order to prove sufficient repeatability of the data [Ref 3]. The "old" data (marked TP1) have been measured with the same model but in a different windtunnel. This check showed an excellent agreement between the "old" and "new" data. To demonstrate this in fig. 4.4.1 a comparison of the intake pressure recoveries plotted versus the normalized intake mass flow WAT is given (SVS1 = "new" ONERA windtunnel data)

As must be expected the pressure recovery of the intake does reduce with angle of attack. This is due to the increasing losses inside the inevitable flow separations at the intake entry. Because this intake has been designed for good supersonic performance too its sidewalls and lip shapes are not as blunted as would be necessary for the suppression or at least the delay of flow separations with high angles of attack. Therefore for angles of attack larger than  $30^\circ$  the flow losses increase strongly up to angles of attack of about  $90^\circ$  degrees above which a slight drop up to  $110^\circ$  degrees can be observed. For a flight Machnumber of  $\text{Ma} = 0.7$  in fig. 4.4.2 the pressure recovery at  $\alpha = 110^\circ$  drops down to a value of about 0.5 at the highest intake mass flow tested. But even at  $\alpha = 70^\circ$  degrees the losses can be as high as 20%. This low total pressure recovery produces substantial thrust losses of the engine behind this intake. These thrust losses must be accounted for in the control of the thrust vectoring nozzle which for a demanded side-force must be deflected to a larger angle than without these losses.

Whereas the total pressure losses at high mass flows are larger than those at low mass flows the opposite is true for the two intake parameters mean swirl and dynamic distortion. In order to visualize these effects in fig. 4.4.3 these parameters are plotted for a low mass flow and in fig. 4.4.4 for a large mass flow.

In fig. 4.4.3 it can be recognized that at the low intake mass flow the pressure recovery up to an angle of attack of  $40^\circ$  degrees is nearly constant for all Mach numbers tested. The minimum pressure recovery is reached for  $\text{Ma} = 0.7$  at an angle of attack of  $110^\circ$  degrees. Its value is about 0.60.

The mean swirl angles at an angle of attack of 20 degrees vary between zero and minus two degrees for all Machnumbers. With increasing angle of attack  $\alpha$  and at a Mach number of  $Ma = 0.3$  the negative swirl angles drop to minus four degrees at  $\alpha = 50^\circ$ , the magnitude of the flow rotation then reduces until at about  $\alpha = 90^\circ$  flow rotation is reversed and reaches swirl angles of  $8^\circ$  at an angle of attack of  $\alpha = 110^\circ$ . At higher flight Machnumbers the angles of attack at which the flow rotation changes its sign and at which the maximum positive swirl angles are reached take on lower and lower angles of attack. The magnitude of the maximum positive swirl angle is steadily increasing with Machnumber. For a flight Mach number of  $Ma = 0.7$  the maximum positive swirl angle is larger than  $10^\circ$ . This magnitude of swirl is probably beyond the capabilities of most modern jet-engines. It is interesting to note that for Mach numbers  $Ma = 0.5$  and  $0.6$  there exists a local minimum in the positive swirl angle between the point of rotation reversal and maximum swirl angle. In addition a strong drop in swirl angle with angle of attack can be observed beyond the angle of attack where the maximum of the positive swirl angle occurs.

The dynamic distortion DC60TA for all Machnumbers is increasing with angle of attack and depicts (except for  $Ma = 0.7$ ) a maximum at about an angle of attack of  $\alpha = 80^\circ$ . For higher angles of attack dynamic distortion is dropping and then increasing again. In the same range of angles of attack a strengthening of negative rotation can be observed followed by a growing positive rotation. The reduction in dynamic distortion seems to be connected to the increasing negative rotation and its increase coincides with the increase in positive rotation.

It is rather obvious that the magnitudes of swirl and dynamic distortion at this low engine mass flow would pose a rather hazardous problem for any jet engine.

At the higher engine mass flow the situation is much more promising (fig. 4.4.4). Between  $\alpha = 20^\circ$  and  $40^\circ$  the pressure recovery is slightly depending on the flight Machnumber because of the change of size of the intake air stream tube. Above  $\alpha = 50^\circ$  the dependency of the strong drop in pressure recovery on Mach number is depicted in this figure. A lowest value in total pressure recovery of  $pt_2/pt_0 = 0.50$  is reached for a Mach number of  $Ma = 0.7$  at an angle of attack of  $\alpha = 110^\circ$ .

The mean swirl angles stay nearly constant at about  $-2^\circ$  for angles of attack of up to  $\alpha = 60^\circ$ . For  $Ma = 0.30$  and increasing angles of attack the magnitude of the negative swirl angle is reduced until at an angle of attack of  $\alpha = 90^\circ$  a reversal of the flow rotation starts and is growing. Finally swirl angles of about  $+8^\circ$  are reached at an angle of attack of  $\alpha = 110^\circ$ . For the other Mach numbers the magnitude of negative swirl angles reaches a maximum negative value at  $\alpha = 80^\circ$ . With further increasing angles of attack these negative swirl angles diminish with a steep gradient. Rotational flow reversal sets in at angles of attack between  $\alpha = 87^\circ$  and  $92^\circ$ . Whereas the positive swirl angles at  $Ma = 0.5$  are very similar to those at  $Ma = 0.3$  the positive swirl angles at  $Ma = 0.6$  and  $0.7$  depict a maximum before they drop again to nearly zero at  $\alpha = 110^\circ$ . Beginning at an angle of attack of  $\alpha = 50^\circ$  negative rotation starts growing until at  $\alpha = 80^\circ$  positive rotation takes over. Negative rotation becomes predominant again at the highest angles of attack.

The values of the dynamic distortion parameter do not reach the high magnitudes as for the low intake mass flow. At least for a Mach number of  $Ma = 0.5$  a similar dependency between dynamic distortion and swirl can be observed as for the low intake mass flow case where an increase in dynamic distortion occurs together with a strengthened negative rotation and a decrease in dynamic distortion is connected to an increase of a positive rotation. Whether or not this dependency is a physical one remains a question to be answered.

Both distortion and swirl depend on the flow into and inside the intake. At the large angles of attack as tested here flow separations can be expected to have a big influence on both parameters. In addition the flow through the bleed slot inside the intake will contribute in their production. So, some clarification of the flow situation inside the intake should be gained when considering in addition the steady state distortion and the throat bleed mass flow. Steady state distortion can be taken as a measure for losses possibly created by flow separations.

For the low intake mass flow these parameters are plotted in fig. 4.4.5 as a function of angle of attack. Comparing steady state and dynamic distortion (see fig. 4.4.3) first it can be recognized that up to an angle of attack of  $\alpha = 50^\circ$  both are increasing. Between  $\alpha = 50^\circ$  and  $\alpha = 70^\circ$  steady state distortion is reducing whereas the dynamic distortion is about constant. For larger angles of attack both show a similar behaviour with a maximum at  $\alpha = 80^\circ$  and a minimum at about  $\alpha = 90^\circ$ . There is a further increase in both parameters up to  $\alpha = 110^\circ$ . However there is a pronounced difference in the magnitude of the two parameters at this maximum angle of attack. Whereas the dynamic distortion values again reach the level of the maximum at about  $\alpha = 80^\circ$  the steady state distortion levels are even lower than those at an angle of attack of  $\alpha = 20^\circ$ .

Bleed mass flow (flow out of the intake) is nearly constant up to an angle of attack of  $\alpha = 50^\circ$ . The increase in distortion in this incidence range can therefore be interpreted as due to an increase in flow losses at the intake entrance. Bleed mass flow is dropping to zero at around  $\alpha = 70^\circ$ . Between  $\alpha = 50^\circ$  and  $\alpha = 70^\circ$  steady state distortion is decreasing. Because the flow losses at the intake entrance will definitely grow in this range it must be concluded that the reduction in bleed mass flow has a positive effect on the distortion. The distortion increase up to  $\alpha = 80^\circ$  is probably due to the increasing flow losses at the intake lip (flow separation). Here the bleed mass flow into the intake is small and cannot be expected to have a noticeable influence into the distortion. However, above  $\alpha = 80^\circ$  the bleed mass flow into the intake seems to be large enough to be responsible for the strong reduction in steady state distortion up to  $\alpha = 90^\circ$ . Above this angle of attack the flow losses inside the lip separation seem to dominate the production of distortion again.

At the high intake mass flow the increase in steady state and dynamic distortion with angle of attack is similar as for the low mass flow case (figs. 4.4.4 and 4.4.6). Depending on the flight Mach number the maximum of the dynamic distortion has been shifted to  $\alpha = 60^\circ$  or higher. Beyond this angle of attack the dynamic distortion seems to possess a sinus-like dependency on angle of attack. At  $\alpha = 110^\circ$  the dynamic distortion values are higher or of the same order of magnitude as at the angle of attack of the maximum. The steady state distortion graph also depicts a sinus-like shape with values

which are somewhat lower at  $\alpha = 110^\circ$  than at the angle of attack of the maximum.

Although the general appearance of the throat bleed mass flow graphs is quite similar to that of the low intake mass flow case (compare fig. 4.4.5 with fig. 4.4.6) their level has been shifted towards smaller or more negative bleed mass flows. There is also a larger difference between the bleed mass flows at different Mach numbers.

Using the same reasoning as before it can be stated that up to  $\alpha = 60^\circ$  the increase in steady state and dynamic distortion is mainly due to the increasing flow losses at the intake entrance and not so much due to the bleed flow which is nearly constant in this area. Up to  $\alpha = 90^\circ/100^\circ$  the bleed flow into the intake probably is responsible for the reduction in steady state and dynamic distortion. Beyond that angle of attack the increase in distortion can be explained by the most likely fully separated intake flow.

In order to analyze in more detail the distortion to be expected in the following the total pressure distribution at the AIP for a flight Mach number of  $Ma = 0.6$  will be looked at. At the high intake mass flow the lines of constant steady total pressures in the AIP (figs. 4.4.7 to 4.4.10) depict a pronounced high and low on opposite sides of the intake duct. From  $\alpha = 20^\circ$  to  $\alpha = 70^\circ$  the positions of these extreme values rotate with angle of attack first in counterclock-wise direction by about 30 degrees. From  $\alpha = 70^\circ$  to  $\alpha = 110^\circ$  these positions rotate back in clockwise direction by about the same angle. With angle of attack not only the level of the total pressures drops considerably but also the gradient between the high and low which reflects itself also in the low steady state distortion values at the highest angles of attack (see fig. 4.4.6). The lines of constant instantaneous total pressures in figs. 4.4.11 and 4.4.12 indicate some radial distortion at a 6 to 5 o'clock position the value of which still needs to be evaluated. Radial distortion can also be recognized in figs. 4.4.13 and 4.4.14 at the same or slightly different angles of attack but for the low intake mass flow.

How angle of attack affects the flow at the entrance of the intake can be deduced from the plots of static wall pressures at two different x-stations. The x-stations are given in fig. 4.4.15. Static pressures at these x-stations all around the intake duct have been plotted for a high and a low intake mass-flow in fig. 4.4.16 and 4.4.17 respectively. On the ramp of the forward X-station (marked "TOP" in the figures) there is a pronounced pressure gradient from inboard to outboard with the maximum on the intake sidewall side. For small angles of attack the static pressure on the cowl lip (called "BOTTOM") at both x-stations is nearly constant. There is a larger pressure drop from the upwind to the downwind x-station for the higher mass-flow. This flow experiences a stronger acceleration with a reduced probability of flow separations. With increasing angles of attack up to about  $\alpha \approx 80^\circ$  the pressure on the cowl lip at the upwind x-station drops much stronger than the pressure at the ramp side. Its magnitude is also lower than at the downwind station. I.e., whereas at the cowl the flow is decelerated the flow on the sidewall, splitter plate and ramp is accelerated. For the low mass-flow and for angles of attack between  $90^\circ$  and  $110^\circ$  the pressures are nearly constant both around the circumference of the intake and between the two x-stations. For the cowl this could be interpreted as the result of a completely separated flow. For the high mass-flow the differences in pressure between the cowl lip and the ramp persist even for very high angles of attack although the differences in pressures become smaller with angle of attack.

The low mass flow pressures at the aft-station between  $\alpha = 80^\circ$  and  $\alpha = 100^\circ$  are nearly constant indicating a fully separated flow.

## 5. CFD investigations

Numerical flow calculations can be used both for the understanding of windtunnel model results and their extrapolation to full-scale free-flight conditions. Understanding of the intake flow is of special importance if proposals would become necessary to improve the intake performance. Therefore parallel to the experimental work described above CFD work has been started on an isolated intake grid model. Due to limited computer power a more complex model comprised of the intake and the fuselage has been envisaged for the future. Because this is an on-going work only results of two Navier-Stokes calculations are presented here to demonstrate the progress accomplished so far. Details of the numerical code used can be found in Ref. [4] and are not repeated here. The code is of a multi-block structured type. The turbulence model applied has been the Baldwin-Lomax model. Two Navier-Stokes grids have been constructed. One grid can be used for the calculation with the cowl lip in the zero position [Ref. 5], i.e. with no gaps between the lip and the sidewalls. In the second grid [Ref. 6] the cowl is set at the most open position as it has been tested during the windtunnel investigations. A grid for such a configuration even today is quite a challenge.

The calculations have been performed for the flow conditions in the windtunnel at a Mach number of  $Ma = 0.6$ . The angle of attack in both calculations was set at  $\alpha = 21.3^\circ$ . In figures 4.4.18 to 4.4.22 some calculation results of both configurations are depicted. The intake mass flow of the intake has been fixed by specifying the same static pressure at the engine face (AIP) for both configurations. As can be seen in figs. 4.4.18 and 4.4.20 the opening of the cowl changes the entrance flow of the intake. The pressure on the ramp is raised. There is much more expansion on the outside of the intake side wall (more side-spillage). The flow into the bleed slot is modified with the large area of local expansion drastically reduced. At the hinge line of the cowl a strong expansion over the whole width of the intake is created (fig. 4.4.22). This expansion produces nearly sonic conditions. At the engine face with the cowl closed (fig. 4.4.19) there is an area of low energy flow (small  $Ma$ ) at the bottom. The flow direction is from top to bottom. The Mach number distribution with the open cowl (fig. 4.4.21) is much more uniform with a nearly horizontal flow direction and some rotation at the top.

## 6. Interpretation of results and conclusions

The magnitude of the intake parameters swirl, steady state, dynamic radial and circumferential distortion characterize intake/engine compatibility. Any engine possesses limits for each of these parameters and combinations thereof. Exceeding of these limits can lead to power loss, engine surge and/or even loss of the engine. Because these limits are different for each modern jet-engine (and usually are restricted) the interpretation of the intake results in the following can be based only on the experience of the intake specialist.

It can be expected that the large swirl angles connected with the high distortion values (both steady state and dynamic) of the low intake mass flow will pose a problem to any jet engine. However it will be unlikely that at very high angles of attack a pilot will throttle down his engine. To prevent an

unintentional throttling back a limiter in the flight control system of the aircraft might be incorporated.

At the high intake mass flow intake/engine compatibility should be ensured up to angles of attack of about  $\alpha \approx 60^\circ$ . Above this angle of attack detailed analysis by the engine manufacturer will be necessary in order to find out whether compatibility problems may arise not. In case of problems it would be possible to either modify the control laws of the engine, to incorporate modifications to the intake or to limit the maximum angle of attack of the aircraft. Modifications to the intake could be a modification of the throat slot bleed mass flow at the high angles of attack and/or a modification of the cowl lip shape that reduces flow separation. Both proposals would be relatively easy to implement. Both modifications could be checked by performing CFD calculations of the intake flow thus reducing necessary windtunnel investigations.

- [4] R.K. Höld,  
Development of the Navier-Stokes Code NSFLEX for Large Scale Numerical Calculation of Steady and Unsteady Flows.  
ASME, International Symposium on Computational Technologies for Fluid/Thermal/Chemical Systems with Industrial Application, San Diego, 1998
- [5] Th. Berens  
Navier-Stokes-Raumnetz für den isolierten EF2000-Einlauf mit Throat Bleed  
Dasa-S-TN-495, 1998
- [6] Th. Berens  
Navier-Stokes-Raumnetz für den isolierten EF2000-Einlauf mit  $26^\circ$  Lippenstellung für Strömungsrechnungen im Hochangstellwinkelbereich  
Dasa-S-TN-524, 1999

## 7. Acknowledgements

The work described in this paper has been performed as part of the company-funded Dasa technology program. Many colleagues both in the Dasa experimental and intake group have contributed. H. Malefakis was the technically responsible for the design of the experimental program and the analysis of the test data. The contribution of ONERA and their specialists is very much appreciated.

## 8. References.

- [1] E. Grigat  
Verbesserung der Flugleistungen von Kampfflugzeugen durch Einsatz von Schubvektorsteuerung  
DGLR-JT99-137, DGLR Jahrestagung Berlin, 1999  
DGLR Jahrbuch 1999
- [2] G. Rauh, M. Jost  
Thrust Vectoring – Growth Potential for Advanced Fighter Aircraft  
7<sup>th</sup> European Propulsion Forum “Aspects of Engine/Airframe Integration”, Pau/France, March 1999
- [3] Malefakis  
Analyse der Ergebnisse der FC10-Einlaufmessung bei hohen Anstellwinkeln im S1 Windkanal der Onera;  
Testphase SVSI  
Dasa-S-TN-578, 27.3.2000

Vari-cowl	M	$\beta$	Fore-plane	Angle of Incidence									
				20°	30°	40°	50°	60°	70°	80°	90°	100°	110°
$\delta_l$	0.3	0°	$\theta_1$	X	X	X	X	X	X	X	X	X	X
		$\pm 10°$	$\theta_1$	X									
	0.50	0°	$\theta_1$	X	X	X	X	X	X	X	X	X	X
	0.60	0°	$\theta_1$	X	X	X	X	X	X	X	X	X	X
		0°	$\theta_2$		X					X			
	0.7	0°	$\theta_1$		X		X		X	X	X		X
	0.8	0°	$\theta_1$	X	X	X	X						

Table 1: Test Program

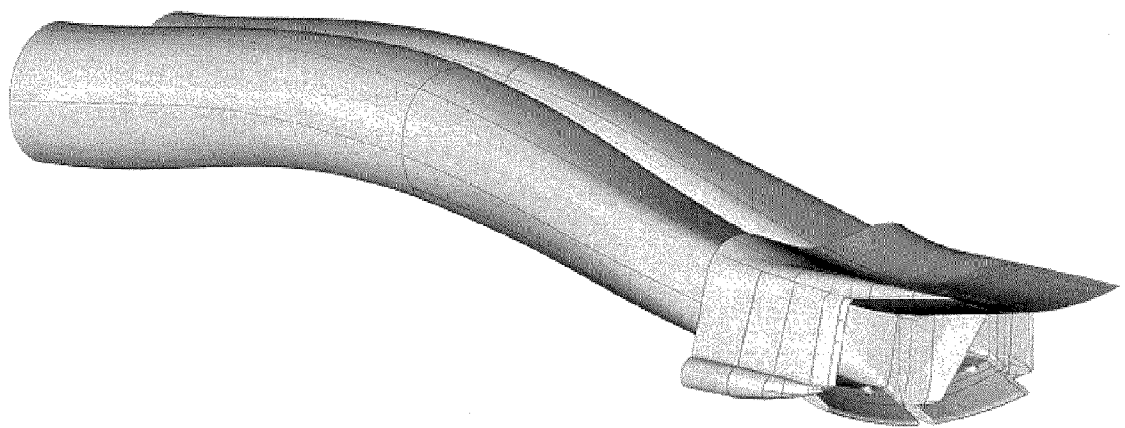


Fig. 3.1 : 3-D View of intakes

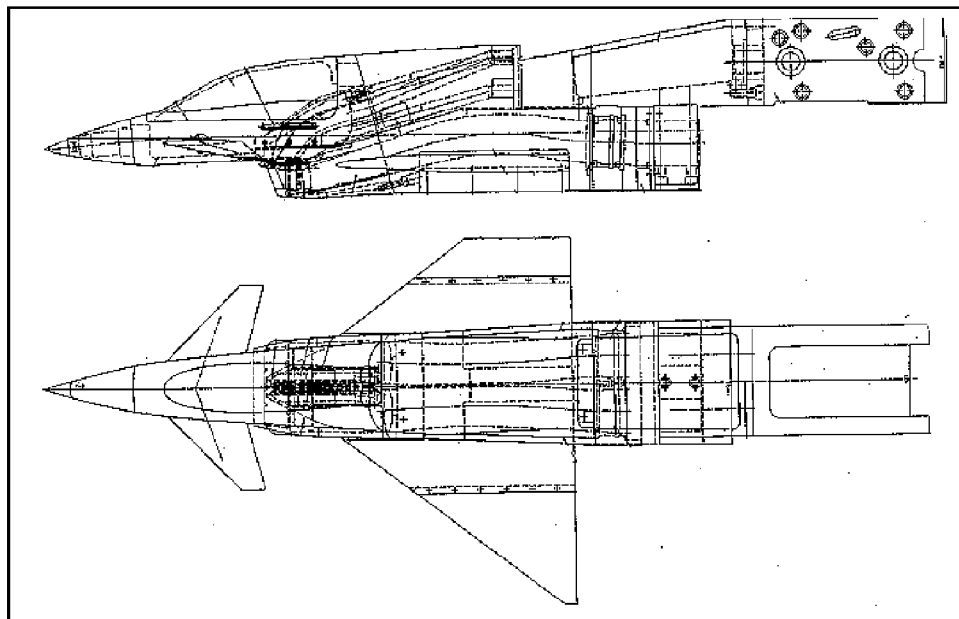


Fig. 4.1.1: Intake Model (1:10.32)

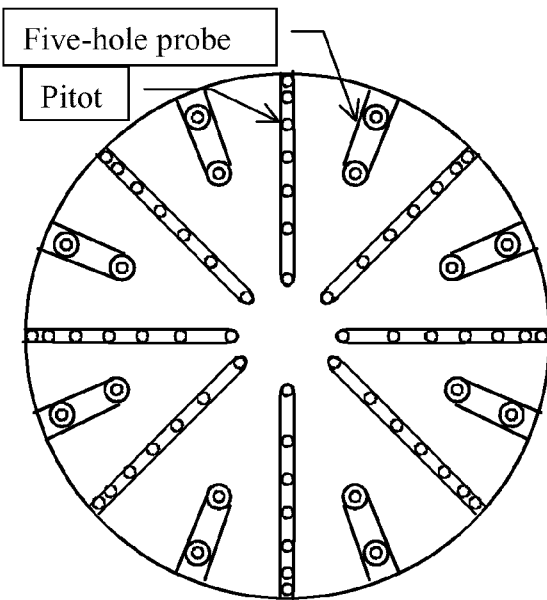
**Port Intake**

Fig.4.3.1: Port AIP Swirl Rake

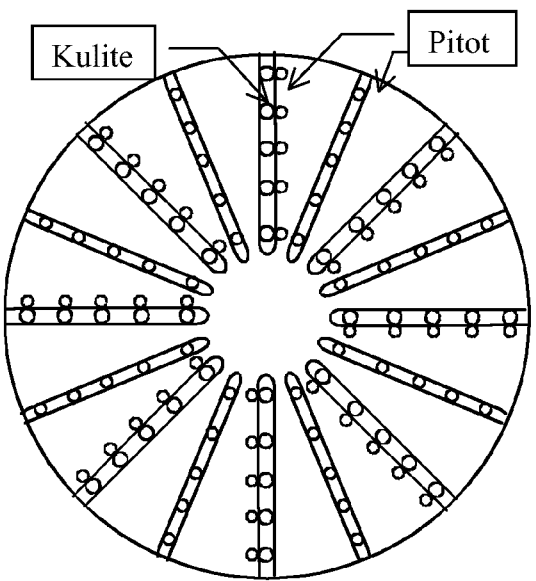
**Stbd Intake**

Fig.4.3.2: Starboard AIP Dynamic Rake

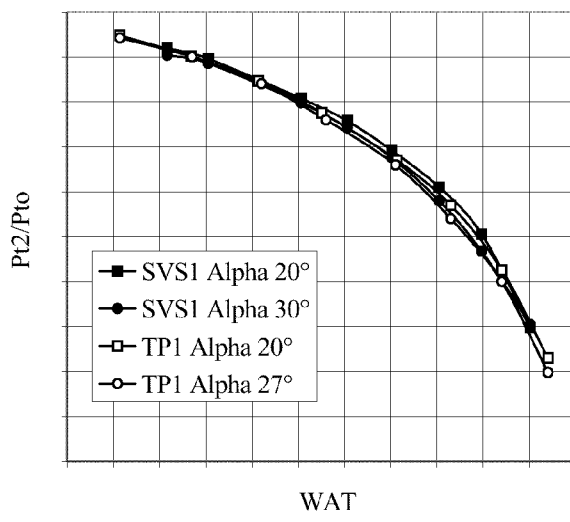
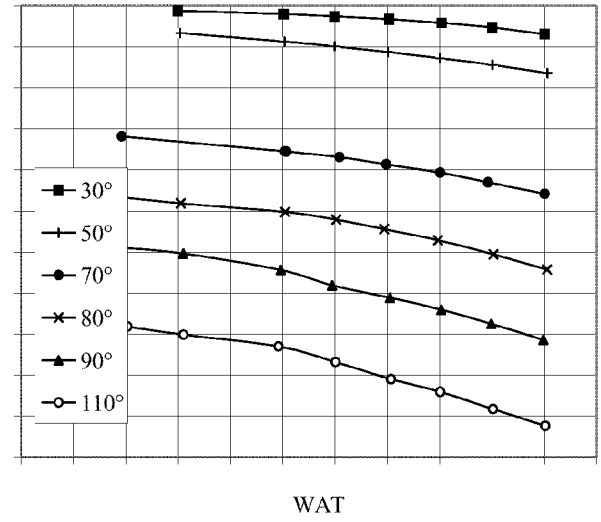


Fig.4.4.1: Repeatability of Pressure Recovery

Fig.4.4.2: Pressure Recovery versus WAT at  $Ma=0,70$

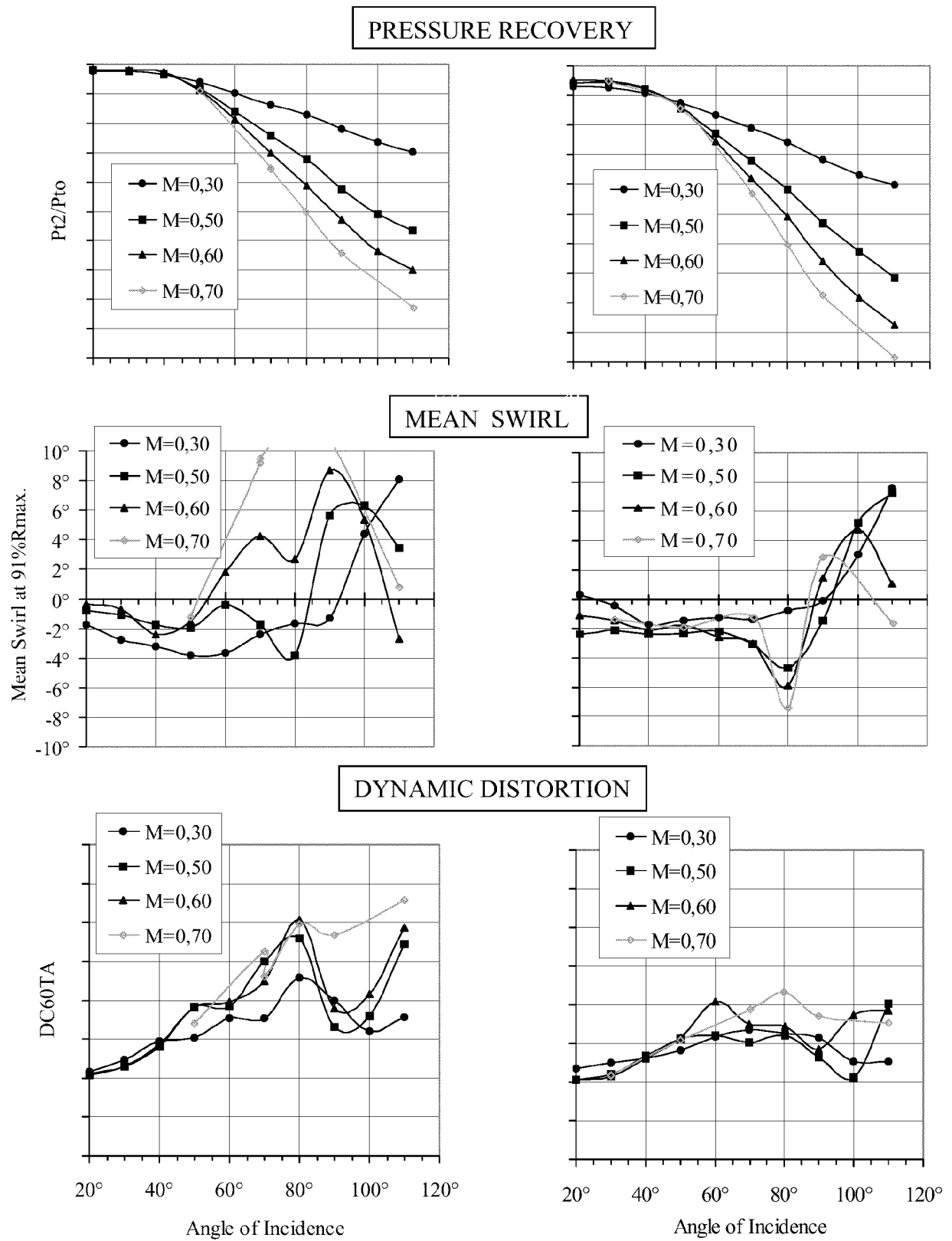


Fig.4.4.3: Pressure Recovery, Swirl and Dynamic Distortion at low WAT

Fig.4.4.4: Pressure Recovery, Swirl and Dynamic Distortion at high WAT

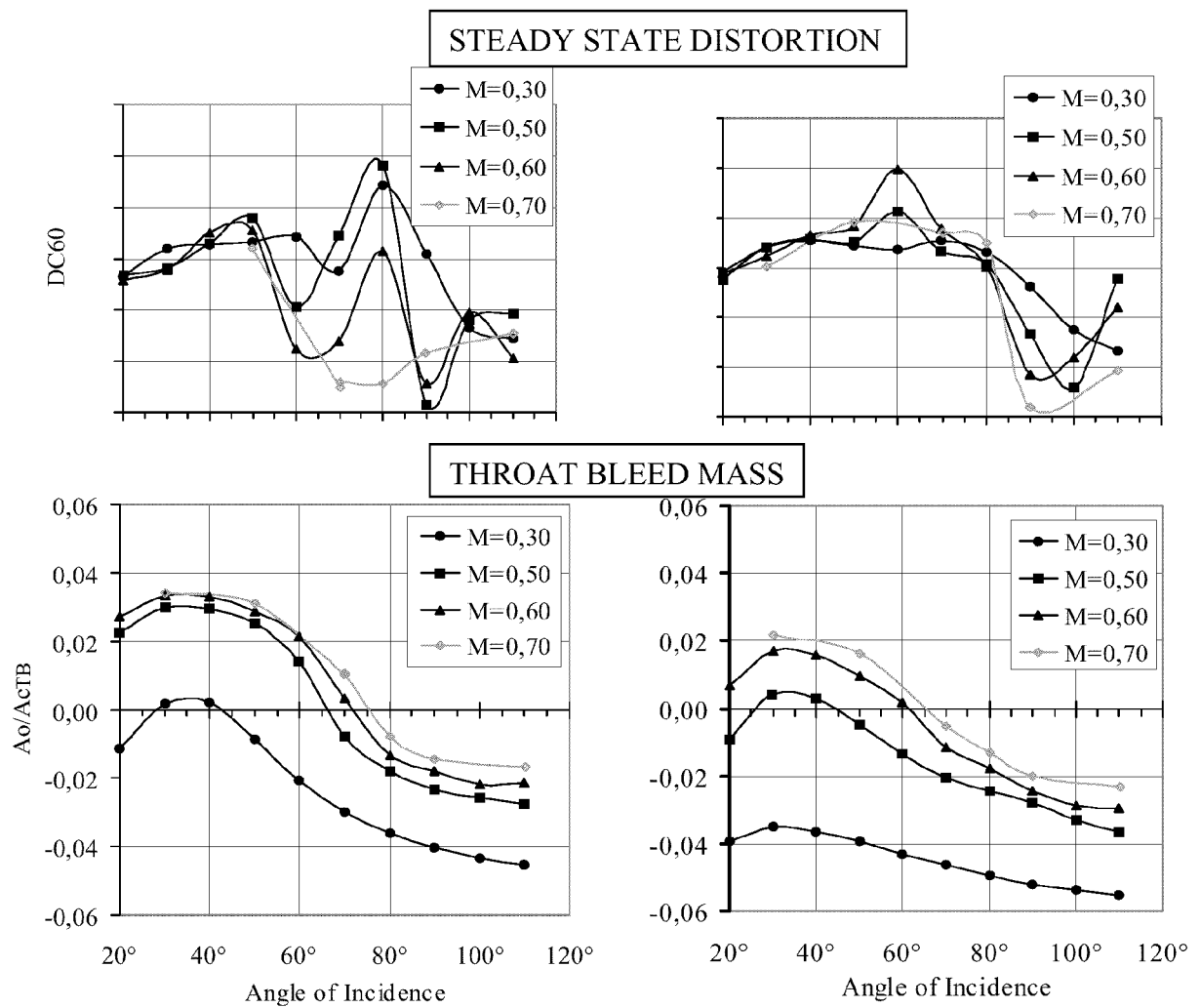


Fig. 4.4.5 Steady State Distortion and Throat Bleed Mass Flow at low WAT

Fig. 4.4.6 Steady State Distortion and Throat Bleed Mass Flow at high WAT

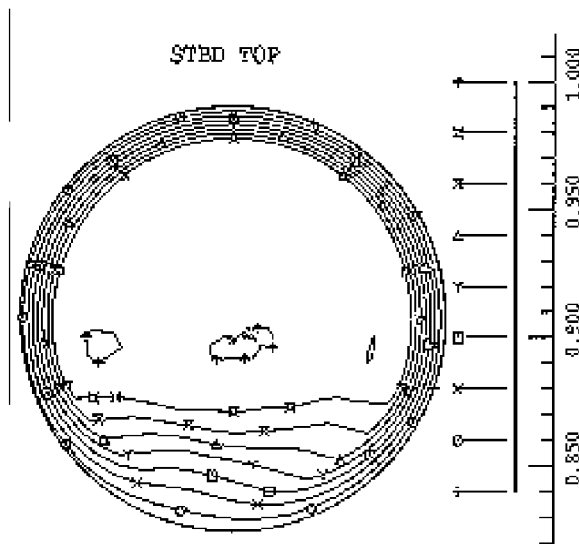


Fig. 4.4.7: Steady State Total Pressures in AIP (Ma = 0.6,  $\alpha = 20^\circ$ , high WAT)

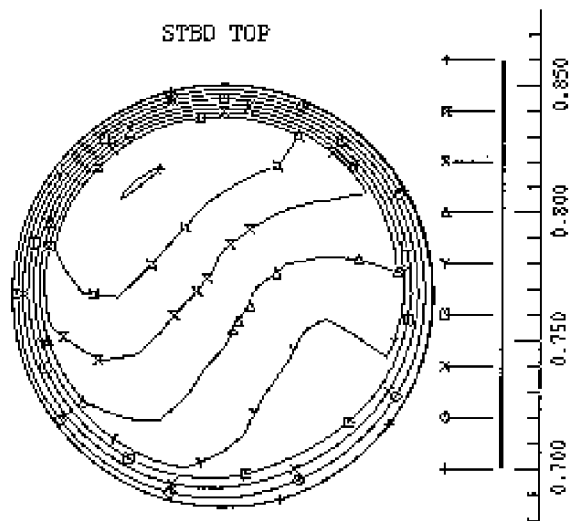


Fig. 4.4.8: Steady State Total Pressures in AIP (Ma = 0.6,  $\alpha = 70^\circ$ , high WAT)

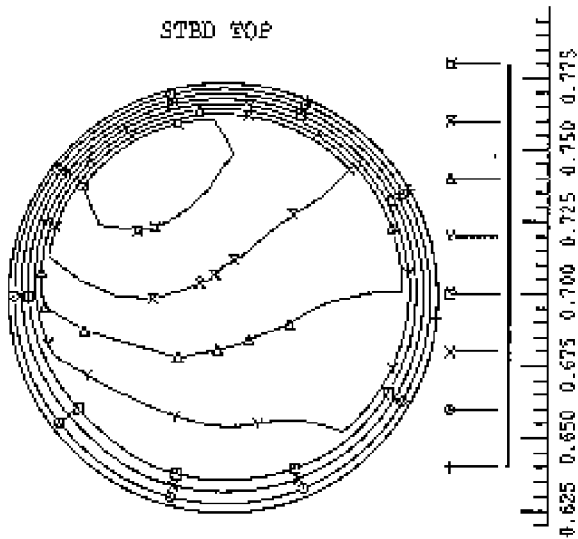


Fig. 4.4.9: Steady State Total Pressures in AIP  
( $Ma = 0.6$ ,  $\alpha = 80^\circ$ , high WAT)

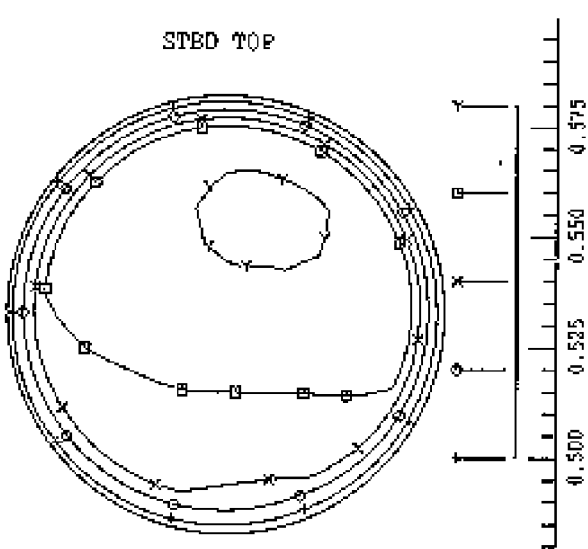


Fig. 4.4.10: Steady State Total Pressures in AIP  
( $Ma = 0.6$ ,  $\alpha = 110^\circ$ , high WAT)

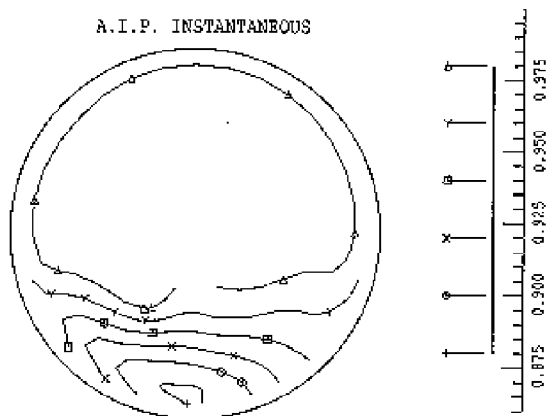


Fig. 4.4.11: Instantaneous Total Pressures in AIP  
( $Ma = 0.6$ ,  $\alpha = 30^\circ$ , high WAT)

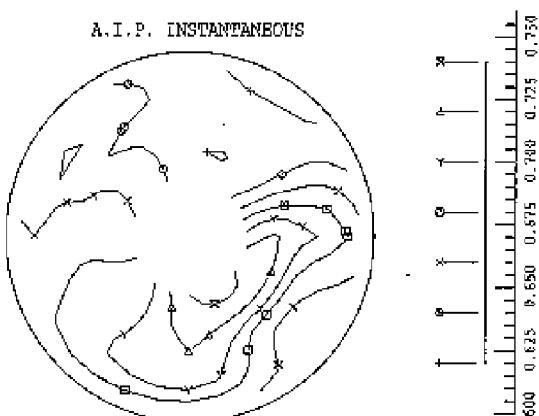


Fig. 4.4.12: Instantaneous Total Pressures in AIP  
( $Ma = 0.6$ ,  $\alpha = 90^\circ$ , high WAT)

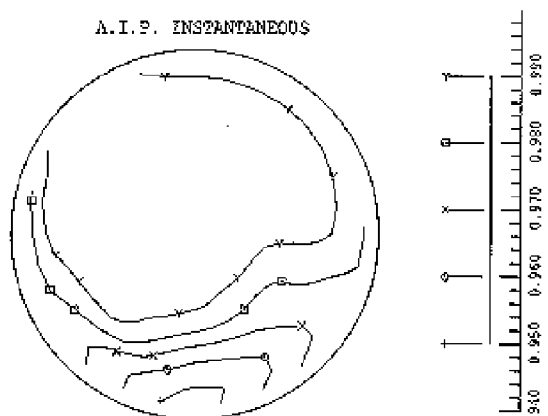


Fig. 4.4.13: Instantaneous Total Pressures in AIP  
( $Ma = 0.6$ ,  $\alpha = 30^\circ$ , low WAT)

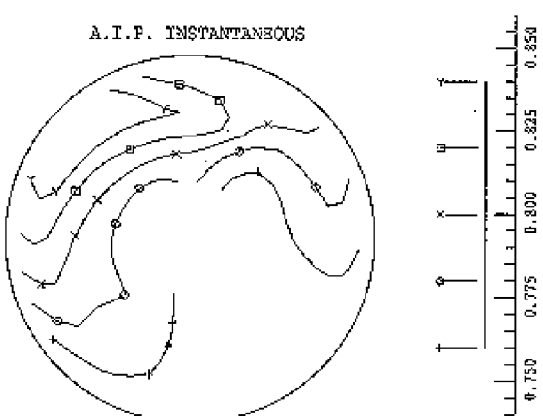


Fig. 4.4.14: Instantaneous Total Pressures in AIP  
( $Ma = 0.6$ ,  $\alpha = 80^\circ$ , low WAT)

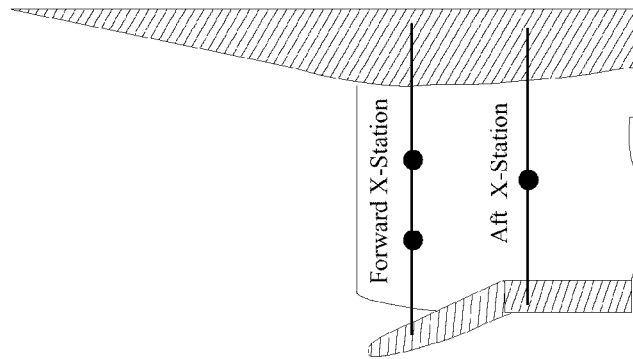


Fig.4.4.15 Position of Pressure Taps at Intake Entrance

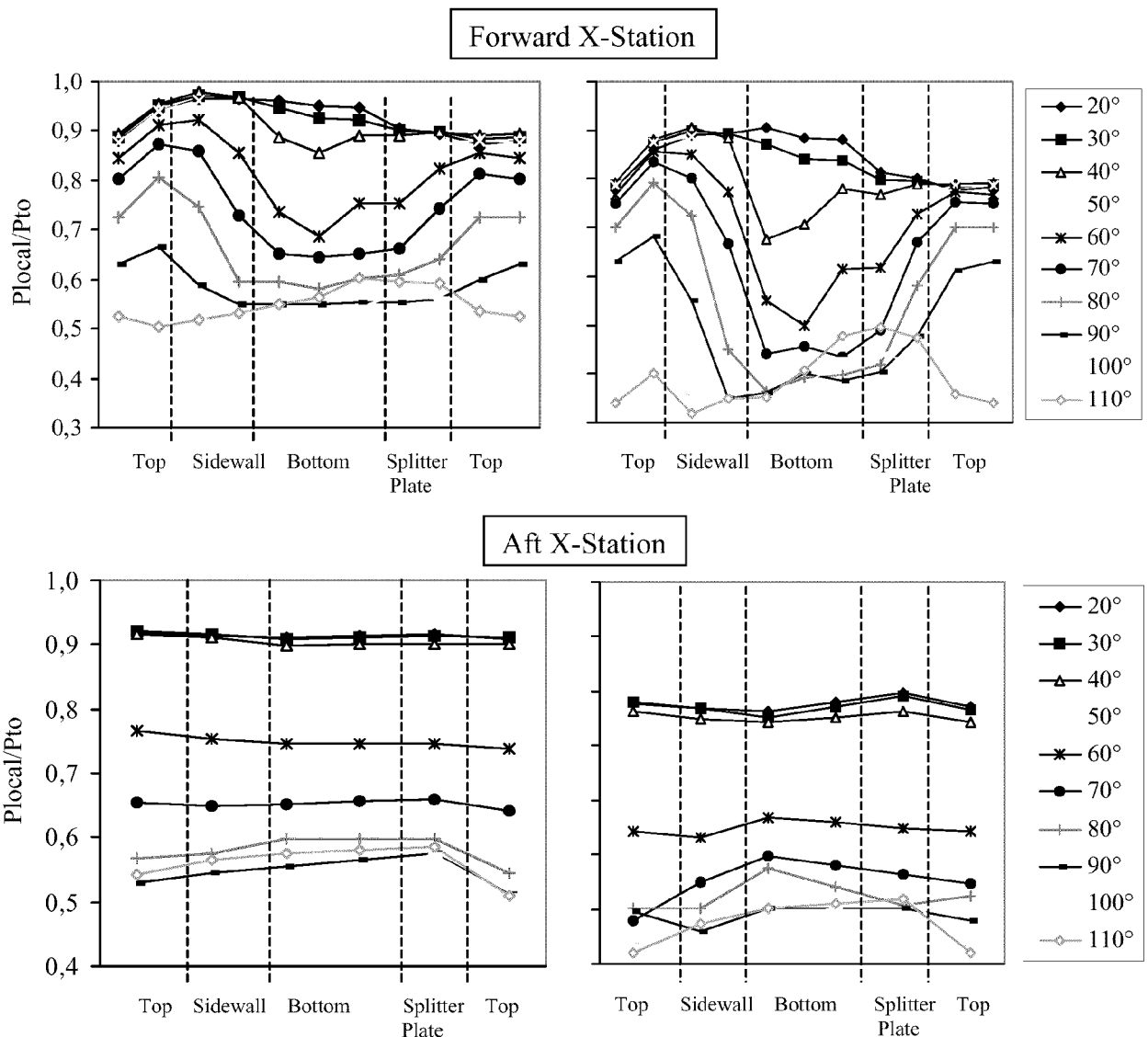


Fig.4.4.16 Static Wall Pressure at Forward and Aft X-Stations (  $Ma=0.6$ , low WAT)

Fig.4.4.17 Static Wall Pressure at Forward and Aft X-Stations (  $Ma=0.6$ , high WAT)

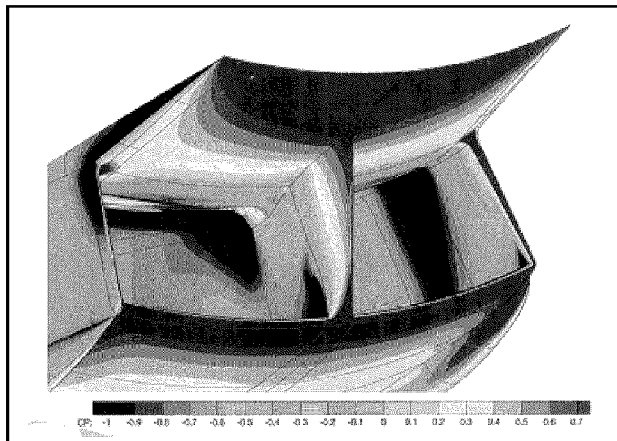


Fig. 4.4.18: Cp at entrance of intake ( $Ma = 0.6$ ,  $\alpha = 21.3^\circ$ )  
- intake lip closed -

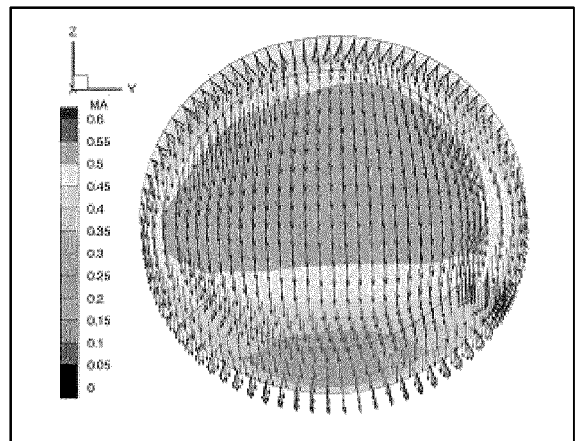


Fig. 4.4.19: Mach and velocity at engine face  
( $Ma = 0.6$ ,  $\alpha = 21.3^\circ$ ) – intake lip closed

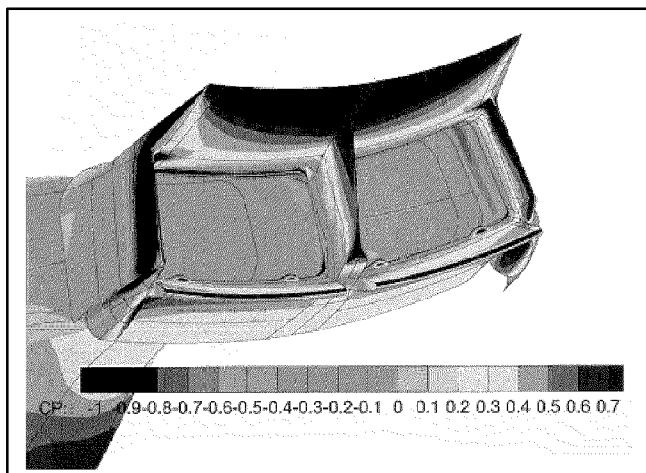


Fig. 4.4.20: Cp at intake entrance ( $Ma = 0.6$ ,  $\alpha = 21.3^\circ$ )  
- intake lip open -

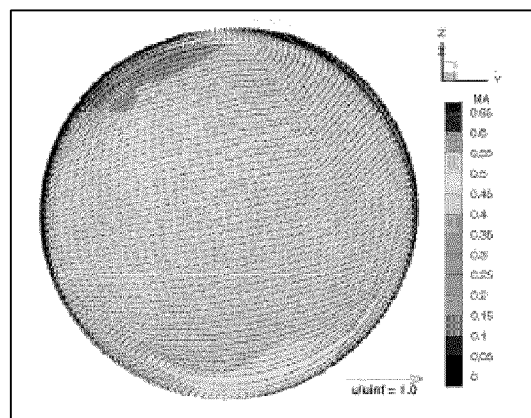


Fig. 4.4.21: Mach and velocity at engine face  
( $Ma = 0.6$ ,  $\alpha = 21.3^\circ$ ) – intake lip open

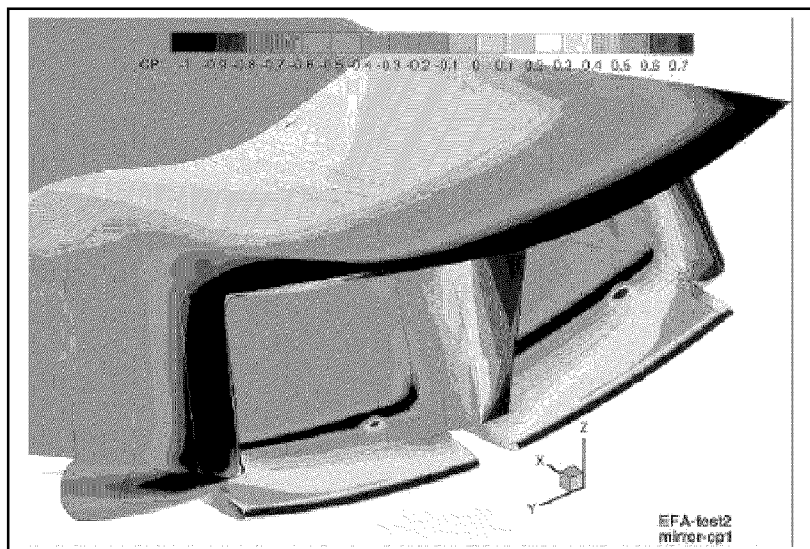


Fig. 4.4.22: Cp at intake entrance ( $Ma = 0.6$ ,  $\alpha = 21.3^\circ$ ) – intake lip open -

Paper#13

Q by Dr. R. Nangia: Relative to canard effects on intake performance - are they properly modeled?

A. (Bissinger): The position of the canard during testing has been at its most downward position as can be seen in the photograph of the model in the wind tunnel. Wind tunnel testing at high angles of attack has proven that the effect of the canard position on the intake performance is negligible.

**This page has been deliberately left blank**

---

**Page intentionnellement blanche**